ELSEVIER

# A dynamic finite volume scheme for large-eddy simulation on unstructured grids

M. Ciardi [a,*], P. Sagaut [b], M. Klein [c], W.N. Dawes [a]

[a] *Department of Engineering, University of Cambridge, Cambridge CB2 1PZ, UK*
[b] *Laboratoire de Modélisation en Mécanique, Université Pierre et Marie Curie, 4 place Jussieu, Boite 162, 75252 Paris Cedex 05, France*
[c] *Energie und Kraftwerkstechnik, TU Darmstadt, Petersenstraße 30 64287 Darmstadt, Germany*

## Abstract

In recent years there has been considerable progress in the application of large-eddy simulation (LES) to increasingly complex flow configurations. Nevertheless a lot of fundamental problems still need to be solved in order to apply LES in a reliable way to real engineering problems, where typically finite-volume codes on unstructured meshes are used. A self-adaptive discretisation scheme, in the context of an unstructured finite-volume flow solver, is investigated in the case of isotropic turbulence at infinite Reynolds number. The Smagorinsky and dynamic Smagorinsky sub-grid scale models are considered. A discrete interpolation filter is used for the dynamic model. It is one of the first applications of a filter based on the approach presented by Marsden et al. In this work, an original procedure to impose the filter shape through a specific selection process of the basic filters is also proposed. Satisfactory results are obtained using the self-adaptive scheme for implicit LES. When the scheme is coupled with the sub-grid scale models, the numerical dissipation is shown to be dominant over the sub-grid scale component. Nevertheless the effect of the sub-grid scale models appears to be important and beneficial, improving in particular the energy spectra. A test on fully developed channel flow at $Re_\tau = 395$ is also performed, comparing the non-limited scheme with the self-adaptive scheme for implicit LES. Once again the introduction of the limiter proves to be beneficial.
© 2005 Elsevier Inc. All rights reserved.

## 1. Introduction

Large-eddy simulation (LES) is an approach to solve the full 3D Navier–Stokes set of equations, which can be located between RANS and DNS in terms of computational cost, accuracy of the solution and amount of information available on the solved flow ([1,2] for a general presentation).

---

* Corresponding author.
  *E-mail address:* mc346@eng.cam.ac.uk (M. Ciardi).

The quality of the LES calculation is the result of the coupling of different aspects, which interact strongly. In particular, the following aspects need to be considered for a given flow configuration:

- The discretisation scheme, which affects any LES solution but becomes also responsible of sub-grid scale closure in the implicit LES approach.
- The sub-grid scale model (for non-implicit LES).
- The explicit filtering procedure (for the modelling approaches that require explicit filtering), and the associated filter function (crucial for the unstructured implementation [3]).
- The mesh quality and resolution.

The interactions of these four aspects have been extensively analysed using different prospectives. In particular, each one of them could be associated with an equivalent filtering operation [4], a component of error (modelling error or numerical error [5]), or a dissipative action on the solved equations. Nevertheless the complexity of the interaction is such that results presented are never general. Therefore, the successful combinations of choices (as the unsuccessful ones!) represent an interesting result, which could contribute to improve the general understanding of LES.

The main goal of this paper is the development of a self-adaptive discretisation scheme in the context of an unstructured finite-volume flow solver. The strategy adopted tries to minimise the contribution of artificial dissipation, relying on a sensor that detects wiggles in the flow variables.

First the scheme is tested with isotropic turbulence at infinite Reynolds number using an implicit LES approach. This is based on the concept of the monotone-integrated large-eddy simulation (MILES) approach proposed by Boris et al. [6]. In this formulation, the energy transfer from the resolved scales to the sub-grid scales is driven by the artificial dissipation of the discretisation scheme. The potentiality of the implicit approach is still to be investigated from the theoretical point of view. Garnier et al. [7] have presented poor results produced with several shock-capturing schemes on decaying isotropic turbulence, showing how the accuracy of the MILES approach is strongly dependant on the specific discretisation scheme used. On the other hand, many satisfactory MILES calculations have been presented during the last decade, often involving complex configurations. Encouraging results have also been presented in the context of an unstructured implementation (see [8]).

The interaction between the self-adaptive discretisation scheme and two different sub-grid scale models is also investigated with isotropic turbulence at infinite Reynolds number. Two levels of mesh resolution are considered, together with an explicit filtering procedure based on the discrete interpolation filters proposed by Marsden et al. [12].

A comparative analysis between numerical dissipation and sub-grid scale dissipation is performed. It is inspired by the theoretical analysis presented by Ghosal [5] and by the analysis on upwind schemes performed by Sengupta and Nair [9]. Ghosal performed a quantitative evaluation of error terms and sub-grid scale terms for an isotropic homogeneous turbulent flow, using the analytic expression of the Von Karman model for the energy spectrum. Differentiation error and aliasing error were considered for different finite difference schemes. The main result is the extreme importance of numerical error in most of the configurations considered. The two main aspects which determine the relative importance of the numerical error over the sub-grid term are the order of accuracy of the scheme and the ratio of filter size over mesh size. In the context of a second order scheme (which is the practical choice for the unstructured implementation), only extremely high values of the ratio of filter size over mesh size guarantee that the sub-grid scale term is dominant. The effect of these high values would be a huge increase in mesh resolution, since the filter size (and the associated filter cutoff) cannot be pushed beyond a certain limit for a specific LES problem. In realistic applications this is not practical, and a dominance of numerical dissipation over the sub-grid scale term is likely to appear in most of the unstructured LES simulations.

Qualitatively similar results were obtained by Chow and Moin [10], who extended Ghosal's analysis using more realistic spectra obtained with a direct numerical simulation (DNS) dataset.

These conclusions are in part mitigated by two aspects. First of all different components of error have different behaviors in spectral space, leading to partial cancellation (as shown by Geurts [14]). In addition, numerical dissipation and sub-grid scale terms are not identical operators in physical space or spectral space, which means that the sub-grid scale term has the freedom to be locally dominant and to impose a long term effect on the discretisation scheme.

Nevertheless the task of the discretisation scheme and of the sub-grid scale model is more complex and ambitious in the context of an unstructured simulation. In principle the former should be a good candidate for implicit LES, since it is quite likely that the role of the sub-grid scale model will not be as strong as in calculations performed with higher-order schemes. The latter should be capable of influencing the discretisation scheme, guiding its effects through long term interactions. Both of these aspects will be investigated in this paper for the discretisation scheme developed and the two sub-grid scale models implemented.

In order to assess the effect of the new discretisation scheme for wall bounded flows, a test on fully developed channel flow at friction Reynolds number $Re_\tau = 395$ has also been performed, comparing the original non-limited scheme and the self-adaptive scheme for implicit LES.

The paper is organized as follows. Governing equations are presented in Section 2. The discretisation scheme and the explicit filtering procedure are introduced in Section 3. The sub-grid scale models are presented in Section 4. Results on isotropic turbulence at infinite Reynolds number and fully developed channel flow at friction Reynolds number $Re_\tau = 395$ are presented in Section 5. Conclusions are drawn in Section 6.

## 2. Governing equations

The LES equations are derived from the Navier–Stokes equations, removing the smallest scales through a filtering operation. In the more general compressible case they contain several subgrid scale terms, but many of these are usually neglected. We consider here only the terms which are kept and modelled, while a more general derivation can be found in [15,16]. The non-dimensionalised Navier–Stokes equations in Cartesian coordinates can therefore be expressed as:

$$\frac{\partial \overline{\rho}}{\partial t} + \frac{\partial (\overline{\rho u_i})}{\partial x_i} = 0,$$

$$\frac{\partial (\overline{\rho u_j})}{\partial t} + \frac{\partial (\overline{\rho u_i u_j})}{\partial x_i} + \frac{\partial \overline{p}}{\partial x_j} = \frac{\partial (\tau_{ij} - \overline{\rho}\tau_{ij}^{\mathrm{r}})}{\partial x_i},$$

$$\frac{\partial (\overline{E})}{\partial t} + \frac{\partial ((\overline{E} + \overline{p})\overline{u_i})}{\partial x_i} = \frac{\partial ((\tau_{ij} - \overline{\rho}\tau_{ij}^{\mathrm{r}})\overline{u_j})}{\partial x_i} - \frac{\partial q_i}{\partial x_i},$$

(1)

where $\overline{\rho}$ and $\overline{p}$ denote, respectively, the filtered density, and the filtered pressure. $\overline{u}$, $\overline{v}$, and $\overline{w}$ denote the Favre-filtered components of velocity. $\overline{E}$ denotes the filtered modified total internal energy (as defined in [15]).

If we denote function $g$ as the LES filtering procedure, the Favre-filtering operation for a generic variable $f$ is defined as:

$$\overline{f} = \frac{g(\rho f)}{g(\rho)}.$$

(2)

The system of equations needs also the equation of state of ideal gas, together with the equation defining the heat fluxes:

$$q_i = -k_{\text{tot}} \frac{\partial \overline{T}}{\partial x_i}, \tag{3}$$

where $\overline{T}$ is the Favre-filtered temperature and the total thermal conductivity $k_{\text{tot}}$ is given by:

$$k_{\text{tot}} = \frac{\gamma \mu}{Pr} + \frac{\gamma \mu_r}{Pr_t}, \tag{4}$$

where $Pr$ is the Prandtl number ($Pr = 0.72$ for air), $Pr_t$ is the turbulent Prandtl number ($Pr_t = 0.6$ for air), $\mu$ is the dynamic viscosity modelled by Sutherland's law and $\mu_r$ is the eddy dynamic viscosity ($\mu_r = \rho v_r$). With this formulation we are imposing a Boussinesq-like model for one of the sub-grid scale terms in the energy equation, through the introduction of the turbulent Prandtl number $Pr_t$.

The viscous stress tensor $\tau$ and the residual stress tensor $\tau^r$ are given by:

$$\tau_{ij} = \mu \left( \frac{\partial \overline{u_i}}{\partial x_j} + \frac{\partial \overline{u_j}}{\partial x_i} \right) + \lambda \delta_{ij} \frac{\partial \overline{u_i}}{\partial x_i}, \tag{5}$$

$$\tau_{ij}^r = \overline{u_i u_j} - \overline{u_i}\,\overline{u_j} \tag{6}$$

with $\delta_{ij}$ the Kronecker delta and the bulk viscosity $\lambda$ defined invoking Stokes' hypothesis:

$$\lambda = -\frac{2}{3}\mu. \tag{7}$$

The eddy kinematic viscosity $v_r$ and the residual stress tensor $\tau^r$ are either provided by the SGS model (for LES calculations) or omitted for ILES (implicit large-eddy simulation).

## 3. Numerical method

The solver used is the Rolls–Royce code HYDRA [21,22]. It is an unstructured finite-volume solver with an edge-based data structure. Time integration is performed using an explicit time-marching procedure, based on the five-stage Runge–Kutta scheme of Martinelli [17].

The spatial discretisation scheme in HYDRA is derived from the MUSCL approach [20], where a functional representation of the flow variables is used in each control volume and Riemann problems are solved at the interfaces. The filtered Navier–Stokes equations can be recast in a semi-discrete compact form, as:

$$\frac{\mathrm{d}Q}{\mathrm{d}t} + R(Q) = 0, \tag{8}$$

where $Q$ is the vector of the conservative variables and $R(Q)$ is the residual vector of the spatial discretisation. Using a finite volume approach the integration of the inviscid and viscous terms over some control volume $\Omega$, after the application of the divergence theorem, gives:

$$R_i^{\mathrm{I}} = \frac{1}{V_i} \oint_{\partial \Omega} \mathscr{F}^{\mathrm{I}}(\mathbf{n}, Q) \, \mathrm{d}S,$$

$$R_i^{\mathrm{V}} = \frac{1}{V_i} \oint_{\partial \Omega} \mathscr{F}^{\mathrm{V}}(\mathbf{n}, Q, \nabla Q) \, \mathrm{d}S, \tag{9}$$

where $V_i$ is the size of the control volume (the median-dual) associated with index $i$, and $\mathscr{F}^{\mathrm{I}}(\mathbf{n}, Q)$ and $\mathscr{F}^{\mathrm{V}}(\mathbf{n}, Q)$ are the inviscid and viscous fluxes in the direction of the unit vector $\mathbf{n}$. For an interior grid point the same fluxes can be discretised as:

$$R_i^{\mathrm{I}} = \frac{1}{V_i} \sum_{j \in E_i} F_{ij}^{\mathrm{I}} \Delta s_{ij},$$

$$R_i^{\mathrm{V}} = \frac{1}{V_i} \sum_{j \in E_i} F_{ij}^{\mathrm{V}} \Delta s_{ij}, \tag{10}$$

where $F_{ij}^{\mathrm{I}}$ and $F_{ij}^{\mathrm{V}}$ are the numerical inviscid and viscous fluxes in the direction $n_{ij}$ associated with the edge connecting node $i$ to node $j$. $E_i$ is the set of all nodes connected to node $i$ via an edge and $\Delta s_{ij}$ is the area associated with the edge considered.

The inviscid flux discretisation is based on the flux-differencing ideas of Roe [18], combining central differencing of the non-linear inviscid fluxes with a smoothing term based on one-dimensional characteristic variables.

$$F_{ij}^{\mathrm{I}} = \frac{1}{2} \left( \mathscr{F}_{ij}^{\mathrm{I}}(Q_i) + \mathscr{F}_{ij}^{\mathrm{I}}(Q_j) + \frac{1}{3} |A_{ij}| \left( \widehat{L}_i^{\mathrm{lp}} - \widehat{L}_j^{\mathrm{lp}} \right) \right),$$

$$A_{ij} = \frac{\partial \mathscr{F}_{ij}^{\mathrm{I}}}{\partial \mathbf{Q}}, \tag{11}$$

where $\widehat{L}^{\mathrm{lp}}$ is a linear transparent pseudo-Laplacian [19]:

$$\widehat{L}_j^{\mathrm{lp}} = \widehat{L}_j - \nabla Q_j \cdot \widehat{L}_j,$$

$$\widehat{L}_j = \left( \sum_{i \in E_j} \frac{1}{|\mathbf{x_i} - \mathbf{x_j}|} \right)^{-1} \sum_{i \in E_j} \frac{Q_i - Q_j}{|\mathbf{x_i} - \mathbf{x_j}|} \tag{12}$$

with $\nabla Q_j$ approximated using the edge weights:

$$\nabla Q_j = \sum_{i \in E_j} \frac{1}{2} (Q_i + Q_j) n_{ij} \Delta s_{ij}. \tag{13}$$

The scheme has also a shock-capturing component which is controlled by a limiter. The limiter is made of a pressure-based coefficient multiplied by the coefficient ($\Phi$) proposed by Ducros et al. [23],

$$\Phi = \frac{\left( \frac{\partial u_i}{\partial x_i} \right)^2}{\left( \frac{\partial u_i}{\partial x_i} \right)^2 + \omega_i \omega_i + \epsilon}, \tag{14}$$

where $\omega$ is the vorticity vector and $\epsilon$ is an arbitrary small number. This limiter ensures robust behavior also on flows with strong unsteadiness. This part of the scheme will not be involved in the modifications proposed in the next section and will not affect the calculations presented in Section 5. For our purposes the scheme is therefore second order accurate.

The viscous fluxes are approximated half-way along each edge and integrated consistently with the inviscid fluxes around each computational cell.

### 3.1. Self-adaptive scheme

The discretisation scheme presented was originally developed for RANS and URANS calculations and is too dissipative for LES (as shown in Section 5). A new version has therefore been developed, introducing a self-adaptive limiter controlled by a sensor. A similar approach has already been successfully applied to a LES solver [24].

$$F_{ij}^{I} = F_{ij}^{I,CD} + S_{ij}F_{ij}^{I,AS}, \tag{15}$$

$F_{ij}^{I,CD}$ and $F_{ij}^{I,AS}$ identify the central differencing component and the artificial smoothing component of the inviscid fluxes already introduced:

$$
\begin{aligned}
F_{ij}^{I,CD} &= \frac{1}{2}\left(\mathscr{F}_{ij}^{I}(Q_i) + \mathscr{F}_{ij}^{I}(Q_j)\right), \\
F_{ij}^{I,AS} &= \frac{1}{6}|A_{ij}|\left(\widehat{L}_i^{lp} - \widehat{L}_j^{lp}\right).
\end{aligned}
\tag{16}
$$

The sensor $S_{ij}$ (associated with the edge $ij$) has to be defined as a function of time and position. The idea is to impose locally the minimum value that keeps the solution stable. A new extended 4-nodes stencil is considered for each edge. This stencil is used at each iteration to check for wiggles in pressure, density, or velocity.

For each edge the stencil is formed selecting on each side another edge among the neighbors. The criterion is to minimise the angle formed by the two edges (angles $\alpha$ and $\beta$ in Fig. 1). In the selection process a maximum value is imposed for $\alpha$ and $\beta$. When the standard stencil does not meet this condition also non-centered stencils are considered (Fig. 2). In this way better quality stencils are obtained. This is true, for instance, when one of the two nodes lies on a boundary, where centered stencils would be too far from forming a straight line (Fig. 3). If along the stencil a wiggle is detected for one of the flow variables, the local value of the sensor is increased, otherwise it is decreased. The sensor $S_{ij}$ at the timestep $n$ is then evaluated as:

$$
Z_{ij}^{n} = 
\begin{cases}
\min\left[\left(Z_{ij}^{n-1} + \Delta_I\right), 1\right] & \text{if a wiggle is detected for the edge } ij, \\
\max\left[\left(Z_{ij}^{n-1} - \Delta_D\right), 0\right] & \text{if a wiggle is not detected for the edge } ij,
\end{cases}
\tag{17}
$$
$$S_{ij}^{n} = C_R Z_{ij}^{n},$$

$Z_{ij}$ is defined in $[0,1]$, while the user defined coefficient $C_R$ has a scaling effect on the sensor and can set its upper limit to a value different from 1. $\Delta_I$ and $\Delta_D$ are the increment and decrement imposed on $Z_{ij}$ when a wiggle is detected or not detected, respectively.

The aim of this improved scheme is to perform as closely as possible to simple central differencing, without incurring in any stability problem. The idea is better explained by a simple one-dimensional convective problem. An arbitrary signal with a given spectrum (from [11]) is convected through the domain, comparing the new self-adaptive scheme, pure central differencing and a TVD scheme (Fig. 4). The $C_R$ coefficient for the self-adaptive scheme is set to 0.08 to match the same value used for the test on isotropic turbulence. The self-adaptive scheme is behaving quite well, producing a spectrum which is closer to the one from central differencing than the TVD scheme. Fig. 5 is comparing the self-adaptive scheme with the original non-limited scheme (with full damping ($C_R = 1.0$) and $C_R = 0.08$). The improvement associated with the
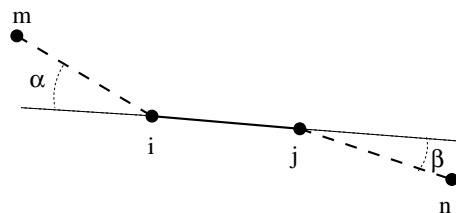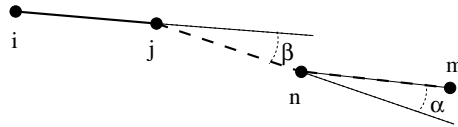


Fig. 1. Standard stencil for the sensor.

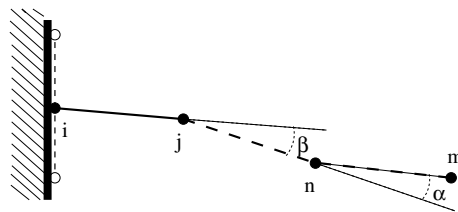Fig. 2. Non-centered stencil for the sensor.



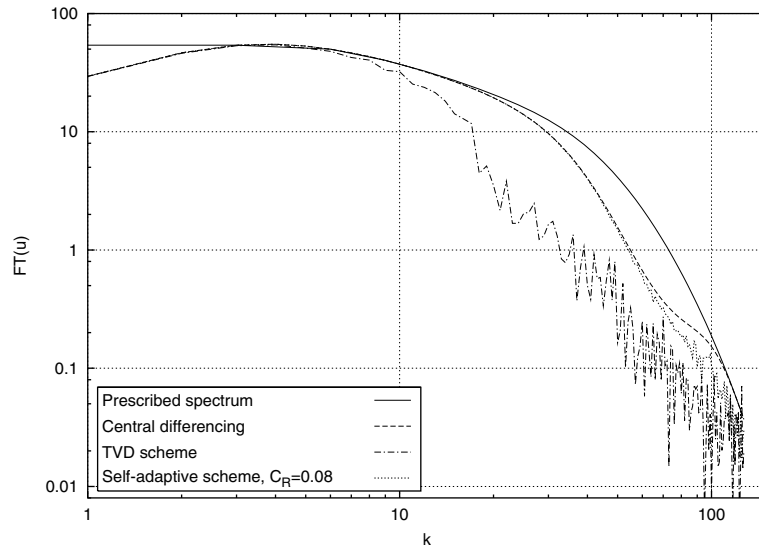Fig. 3. Stencil for an edge with a node on a boundary.



Fig. 4. One-dimensional convective test, comparison of different discretisation schemes.

self-adaptive scheme is evident. This new discretisation scheme is obviously a better candidate to perform LES calculations. The aim of the tests that will be performed is to assess its potential as implicit LES method end also to determine if it could be effectively coupled with existing sub-grid scale models.

### 3.2. Discrete interpolation filter

The dynamic Smagorinsky sub-grid scale model introduced in the following section needs an explicit filtering procedure. The approach implemented is based on the discrete interpolation filters proposed by Marsden et al. [12,13]. This approach can be tuned to achieve a specific order of accuracy for the commutation error, while retaining the possibility to use a variable filter size and unstructured grids. In this implementation, second order has been imposed to match the order of accuracy of the discretisation scheme in
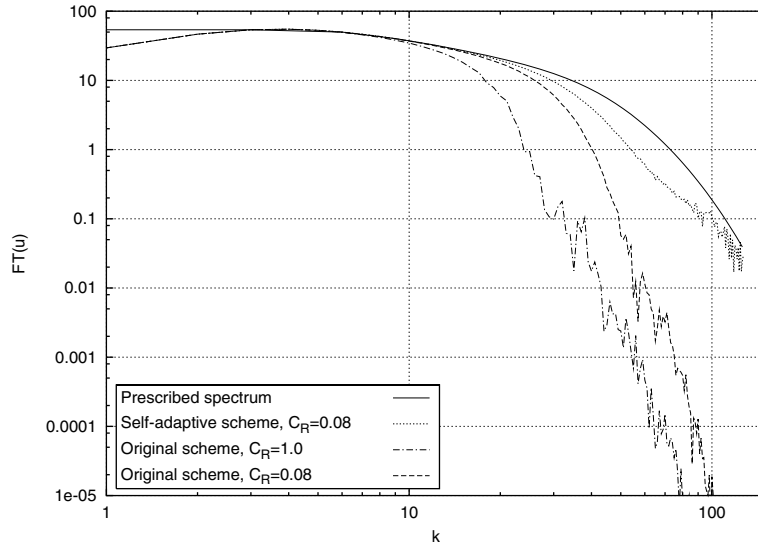
Fig. 5. One-dimensional convective test, comparison between original scheme and new self-adaptive scheme.

use. The filter is expressed as a linear combination of five basic filters. Each basic filter gives second order accuracy, while the linear combination of the basic filters is optimising for the shape and the size of the filter.

The starting point for constructing a basic filter is the definition of its moments $m^{\alpha\beta\gamma}$:

$$m^{\alpha\beta\gamma}(\mathbf{x}) = \frac{1}{\Delta^3(\mathbf{x})} \int \int \int \eta_1^{\alpha}\eta_2^{\beta}\eta_1^{\gamma}G(\mathbf{x},\boldsymbol{\eta})\,\mathrm{d}\eta_1\,\mathrm{d}\eta_2\,\mathrm{d}\eta_3, \tag{18}$$

where $G$ is the kernel of the filter, $\Delta$ is the filter size and the integration is performed over the whole three-dimensional domain. The commutation error of a basic filter can in fact be expressed as a function of its moments (as shown in [1]). In particular, in order to achieve second order commutation error, the following conditions must be met:

$$m^{\alpha\beta\gamma}(\mathbf{x}) = \begin{cases} 1 & \text{if } \alpha = \beta = \gamma = 0, \\ 0 & \text{if } (\alpha + \beta + \gamma) = 1. \end{cases} \tag{19}$$

A basic filter that respects these conditions can be easily constructed using four points (a tetrahedron). If $\mathbf{x}^0$ is the node where we want to filter the flow variables, we can consider the first order polynomial that passes through the four nodes $\mathbf{x}^A$, $\mathbf{x}^B$, $\mathbf{x}^C$ and $\mathbf{x}^D$. If we take the four interpolation weights, needed to interpolate this polynomial on the node $\mathbf{x}^0$, as filtering weights $(w_A, w_B, w_C, w_D)$, we have automatically set to zero all the discrete first order moments:

$$\begin{aligned}
m^{100}(\mathbf{x}^0) &= w_A(x_1^A - x_1^0) + w_B(x_1^B - x_1^0) + w_C(x_1^C - x_1^0) + w_D(x_1^D - x_1^0) = 0, \\
m^{010}(\mathbf{x}^0) &= w_A(x_2^A - x_2^0) + w_B(x_2^B - x_2^0) + w_C(x_2^C - x_2^0) + w_D(x_2^D - x_2^0) = 0, \\
m^{001}(\mathbf{x}^0) &= w_A(x_3^A - x_3^0) + w_B(x_3^B - x_3^0) + w_C(x_3^C - x_3^0) + w_D(x_3^D - x_3^0) = 0,
\end{aligned} \tag{20}$$

We have also set to one the zeroth order moment $m^{000}$:

$$m^{000} = w_A + w_B + w_C + w_D = 1. \tag{21}$$

The other condition to be met by each basic filter imposes that the central node $\mathbf{x}^0$ must be inside the tetrahedron. In order to select the basic filters for a specific node, a list of neighboring nodes is formed at first.

Among the tetrahedra which meet the above conditions, a selection is made, preferring the tetrahedra that have the central node closer to their centroid. The number of neighbors can be changed through a control parameter and has an important effect on the final filter obtained. A small number is going to compromise more on the distance between the centroid and the central node, forcing on the other hand the filter to be more local in physical space. A large number would instead minimise the distance between the centroids and the central node, but would also make the filter less local in physical space. In our implementation we select in the first phase eight basic filters instead of five. In this way we are able to impose a further selection for the best filter (which is constructed using only five basic filters).

The second phase of the process chooses the best combination of basic filters (among the 56 possibilities) and assigns a weight to the central node and to each tetrahedron ($\beta_i$). This is achieved imposing conditions for shape and filter-size to the second order moments. If we prescribe the filter to match an equivalent isotropic spherical top hat filter with filter-size $\Delta$, we obtain the following values to be imposed to the second order moments:

$$
\begin{aligned}
M^{200} &= \frac{3}{4\pi\Delta^3} \int_0^{2\pi} \mathrm{d}\varphi \int_{-\frac{\pi}{2}}^{\frac{\pi}{2}} \mathrm{d}\theta \int_0^{\Delta} r^4 \cos^3\theta \cos^2\varphi \, \mathrm{d}r = \frac{3}{10}\Delta^2, \\
M^{020} &= \frac{3}{4\pi\Delta^3} \int_0^{2\pi} \mathrm{d}\varphi \int_{-\frac{\pi}{2}}^{\frac{\pi}{2}} \mathrm{d}\theta \int_0^{\Delta} r^4 \cos^3\theta \sin^2\varphi \, \mathrm{d}r = \frac{3}{10}\Delta^2, \\
M^{002} &= \frac{3}{4\pi\Delta^3} \int_0^{2\pi} \mathrm{d}\varphi \int_{-\frac{\pi}{2}}^{\frac{\pi}{2}} \mathrm{d}\theta \int_0^{\Delta} r^4 \cos\theta \sin^2\theta \, \mathrm{d}r = \frac{3}{10}\Delta^2, \\
M^{110} &= \frac{3}{4\pi\Delta^3} \int_0^{2\pi} \mathrm{d}\varphi \int_{-\frac{\pi}{2}}^{\frac{\pi}{2}} \mathrm{d}\theta \int_0^{\Delta} r^4 \cos^3\theta \cos\varphi \sin\varphi \, \mathrm{d}r = 0, \\
M^{101} &= \frac{3}{4\pi\Delta^3} \int_0^{2\pi} \mathrm{d}\varphi \int_{-\frac{\pi}{2}}^{\frac{\pi}{2}} \mathrm{d}\theta \int_0^{\Delta} r^4 \cos^2\theta \sin\theta \cos\varphi \, \mathrm{d}r = 0, \\
M^{011} &= \frac{3}{4\pi\Delta^3} \int_0^{2\pi} \mathrm{d}\varphi \int_{-\frac{\pi}{2}}^{\frac{\pi}{2}} \mathrm{d}\theta \int_0^{\Delta} r^4 \cos^2\theta \sin\theta \sin\varphi \, \mathrm{d}r = 0.
\end{aligned}
\tag{22}
$$

Therefore, each of the 56 possible combinations of five basic filters, among the eight initially selected, results in imposing the following system of equations:

$$
\begin{aligned}
m_1^{200}\beta_1 + m_2^{200}\beta_2 + m_3^{200}\beta_3 + m_4^{200}\beta_4 + m_5^{200}\beta_5 &= M^{200}, \\
m_1^{020}\beta_1 + m_2^{020}\beta_2 + m_3^{020}\beta_3 + m_4^{020}\beta_4 + m_5^{020}\beta_5 &= M^{020}, \\
m_1^{002}\beta_1 + m_2^{002}\beta_2 + m_3^{002}\beta_3 + m_4^{002}\beta_4 + m_5^{002}\beta_5 &= M^{002}, \\
m_1^{110}\beta_1 + m_2^{110}\beta_2 + m_3^{110}\beta_3 + m_4^{110}\beta_4 + m_5^{110}\beta_5 &= M^{110}, \\
m_1^{101}\beta_1 + m_2^{101}\beta_2 + m_3^{101}\beta_3 + m_4^{101}\beta_4 + m_5^{101}\beta_5 &= M^{101}, \\
m_1^{011}\beta_1 + m_2^{011}\beta_2 + m_3^{011}\beta_3 + m_4^{011}\beta_4 + m_5^{011}\beta_5 &= M^{011}, \\
\beta_0 + \beta_1 + \beta_2 + \beta_3 + \beta_4 + \beta_5 &= 1,
\end{aligned}
\tag{23}
$$

where $\beta_i$ is the weight associated with the $i$th basic filter, with the exception of $\beta_0$ being the weight of the central node that can be specified by the user. These systems are overspecified and have to be solved using least square approximation. The selection among the 56 possible combinations is made choosing the filter that is closer to be a positive filter. This is achieved evaluating for each combination the minimum node

coefficient among the 20 nodes forming the filter, and then selecting the combination with the biggest value. The second phase of the process, where the weights for the basic filters are computed, is computationally negligible compared with the first phase, where the basic filters are selected. Therefore, the increased accuracy of this implementation has a penalization of approximately 60% in the initial selection process compared with the original approach. This could be reduced compromising on the number of neighboring nodes used during the first phase.

## 4. Sub-grid scale models

The set of equations presented in Section 2 leaves to the sub-grid scale model the task of defining the residual stress tensor $\tau^r$ and the eddy kinematic viscosity $v_r$. A large collection of sub-grid scale models has been produced in the last decades ([1] presents an overview). Two sub-grid scale models are considered in this work together with the implicit approach.

### 4.1. Smagorinsky model

In the Smagorinsky model, a linear eddy viscosity equation relates the residual stress tensor $\tau^r$ to the filtered rate of strain $\overline{S}$ [25].

$$\tau_{ij}^r - \frac{\delta_{ij}}{3}\tau_{kk}^r = -2v_r\overline{S_{ij}}, \tag{24}$$

$$\overline{S_{ij}} = \frac{1}{2}\left(\frac{\partial \overline{u_i}}{\partial x_j} + \frac{\partial \overline{u_j}}{\partial x_i}\right). \tag{25}$$

The eddy kinematic viscosity $v_r$ is modelled by analogy to the mixing-length hypothesis, with a mixing length taken proportional to the filter size $\overline{\Delta}$:

$$v_r = \left(C_s\overline{\Delta}\right)^2\sqrt{2\overline{S_{ij}}\,\overline{S_{ij}}}, \tag{26}$$

where $C_s$ is the Smagorinsky coefficient. Its value is not general and needs to be tailored to the specific kind of flow considered. This guarantees that the right amount of resolved kinetic energy is dissipated in the whole domain, while the same is not true locally. Moreover, the residual stress tensor $\tau^r$ is not modelled correctly and only its global dissipative effects are addressed (for this reason it is classified among functional models in [1]). For isotropic turbulence at infinite Reynolds number the theoretical value of the Smagorinsky coefficient $C_s$ is 0.18.

### 4.2. Dynamic Smagorinsky model

The dynamic Smagorinsky model was originally introduced by Germano [26] and is based on the Smagorinsky model. It provides a methodology for determining an appropriate local value of the Smagorinsky coefficient, which is estimated using the resolved scales. It is based on Germano's identity:

$$\widetilde{\overline{u_i}\,\overline{u_j}} - \widetilde{\overline{u_i}}\,\widetilde{\overline{u_j}} = t_{ij}^r - \widetilde{\tau_{ij}^r}, \tag{27}$$

where

$$\begin{aligned}\tau_{ij}^r &= \overline{u_i u_j} - \overline{u_i}\,\overline{u_j},\\ t_{ij}^r &= \widetilde{\overline{u_i u_j}} - \widetilde{\overline{u_i}}\,\widetilde{\overline{u_j}}.\end{aligned} \tag{28}$$

The tilde symbol $\sim$ indicates the test filtering operation, which is associated with a filter size $\widetilde{\overline{\Delta}}$ (with $\widetilde{\overline{\Delta}} > \overline{\Delta}$ and in general taken $\widetilde{\overline{\Delta}} = 2\overline{\Delta}$). The tensor $t^{\mathrm{r}}$ is the residual stress tensor corresponding to the test filtering level. The left-hand side of Germano's identity is directly computed by filtering the resolved LES velocity field, while for the terms on the right-hand side the Smagorinsky model gives:

$$
\begin{aligned}
\tau_{ij}^{\mathrm{r}} - \frac{\delta_{ij}}{3}\tau_{kk}^{\mathrm{r}} &= -2\left(C_{\mathrm{s}}\overline{\Delta}\right)^2 \overline{S_{ij}}\sqrt{2\overline{S_{ij}}\,\overline{S_{ij}}}, \\
t_{ij}^{\mathrm{r}} - \frac{\delta_{ij}}{3}t_{kk}^{\mathrm{r}} &= -2\left(C_{\mathrm{s}}\widetilde{\overline{\Delta}}\right)^2 \widetilde{\overline{S_{ij}}}\sqrt{2\widetilde{\overline{S_{ij}}\,\overline{S_{ij}}}}.
\end{aligned}
\tag{29}
$$

Substituting into Germano's identity (Eq. 27), we obtain five independent equations for the unknown squared Smagorinsky coefficient $C_{\mathrm{s}}^2$. These can be solved using least square approximation, as proposed by Lilly [27]. In order to guarantee stable behavior a local averaging of $C_{\mathrm{s}}^2$ is also performed. This approach could in principle produce some backscatter, but to avoid instabilities the constant is clipped in order to maintain positive total viscosity (kinematic viscosity $v$ plus eddy kinematic viscosity $v^{\mathrm{r}}$).

### 4.3. Implicit LES

In the implicit approach the residual stress tensor $\tau^{\mathrm{r}}$ is neglected, relying on the assumption that the discretisation scheme is capable of introducing the right amount of dissipation. The idea is based on the concept of the monotone-integrated large-eddy simulation (MILES) approach proposed by Boris et al. [6]. The general implementation uses a blend between two different mechanisms of computing the convective fluxes: a high order flux function and a low order flux function. The latter is usually the shock-capturing component of the scheme. In our implementation the shock-capturing component is only used to deal with compressibility. The high order flux function is the second-order central differencing component, while the dissipation is introduced by the artificial smoothing, which is controlled by a limiter (through the sensor presented in Section 3), and it is also second-order accurate by construction.

A rigorous justification of the MILES approach, in the context of flux limiting discretisation, was presented by Fureby and Grinstein [28–30]. Imposing simplifying assumptions, they derived an expression for the equivalent residual stress tensor, starting from an estimation of the truncation error. The analysis shows how within the limits of the assumptions imposed, the MILES approach can be seen as a blend of a subgrid viscosity component with tensorial viscosity and a component similar to the Leonard tensor. The latter is also equivalent to the sub-grid scale tensor in the scale similarity model (SSM) proposed by Bardina et al. [31], which can be coupled with an eddy-viscosity model to produce a mixed-model.

## 5. Results

Two testcases have been considered: decaying isotropic turbulence and a fully developed channel flow. First a set of calculations of decaying incompressible isotropic turbulence at infinite Reynolds number has been performed. Simulations are initialised using a random solenoidal velocity field with Gaussian kinetic energy spectrum:

$$
E(k) = k^4 \mathrm{e}^{-\frac{2k^2}{k_0^2}}, \quad k_0 = 4, \quad k^2 = k_1^2 + k_2^2 + k_3^2.
\tag{30}
$$

Two different mesh resolutions are considered ($32^3$ and $64^3$), together with the following LES approaches:

- Implicit large-eddy simulation (without any sub-grid scale model).
- Smagorinsky model.
- Dynamic Smagorinsky model.

The filter size has been taken as twice the local edge length. The test filter size has been taken as twice the LES filter size for the dynamic approach.

A preliminary set of calculations has been performed without any sub-grid scale model, in order to assess the behavior of the new discretisation scheme. Three different versions of the scheme are considered:

- The original approach without limiter ($C_R = 1.0$).
- A modified version of the original approach, where the sensor is not used, but artificial dissipation is reduced to 8% of the original amount ($C_R = 0.08$).
- The new self-adaptive scheme with $C_R = 0.08$ and $\Delta_I = \Delta_D = 0.2$.

A calculation without any artificial dissipation contribution ($C_R = 0.0$) was also considered, but became unstable after few iterations as expected.

Figs. 6–8 show the time history of resolved turbulent kinetic energy, enstrophy and the compensated turbulent kinetic energy spectra at the final stage of the computations, using the $32^3$ grid. There is a significant scatter in the theoretical values presented for the decay rate of kinetic energy. Lesieur [32] refers to values in the range between $t^{-1.2}$ and $t^{-1.43}$. The two calculations with the original scheme have for a short length of time a decay rate within the range of the theoretical values but then present a non-physical plateau. The same non-physical plateau appears in the time histories of enstrophy. This spurious feature is removed by the limited scheme, even if now the decay rate is a bit too high ($t^{-1.61}$). The energy spectrum shows a good behavior for the calculation with the self adaptive scheme. The slope is slightly higher than $-5/3$. There is also a moderate pile up of energy at the highest wavenumbers, but the introduction of sub-grid scale models is expected to correct this aspect. A proper tuning of the parameters controlling the limiter could probably act in the same direction, optimising the scheme for implicit LES. This optimization has not been performed so far. The original scheme is obviously overdissipative, even when $C_R$ is reduced to 0.08.
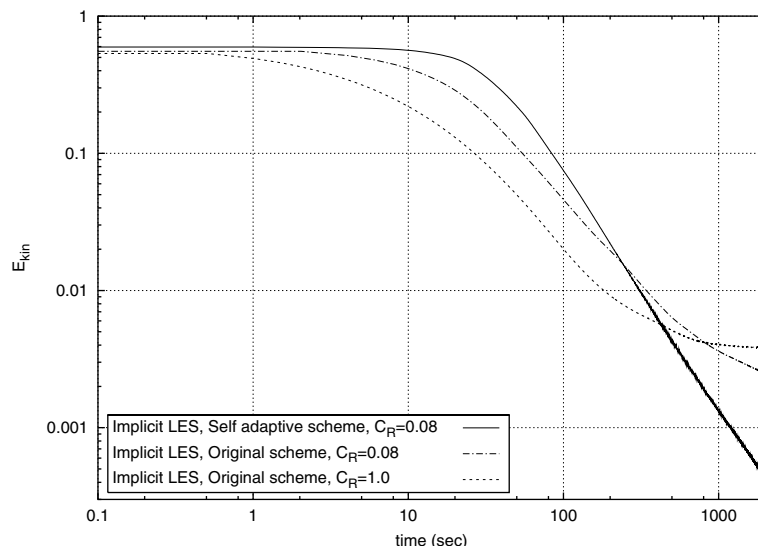


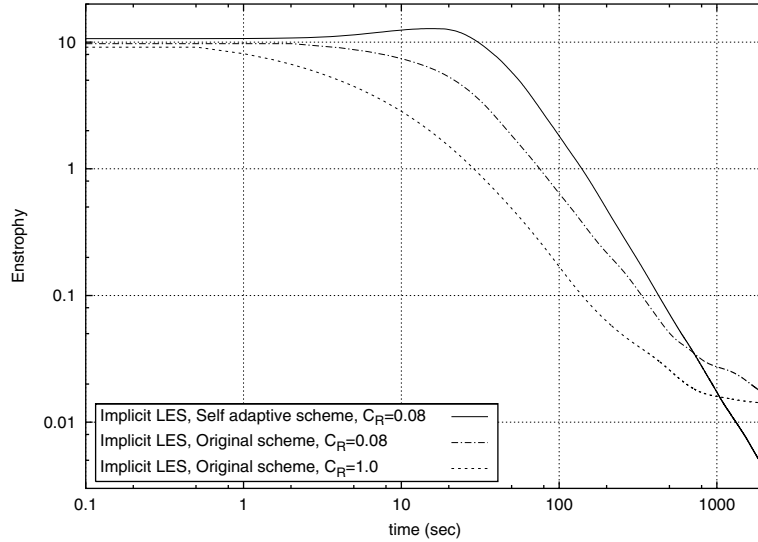Fig. 6. Time history of resolved turbulent kinetic energy – $32^3$ grid.

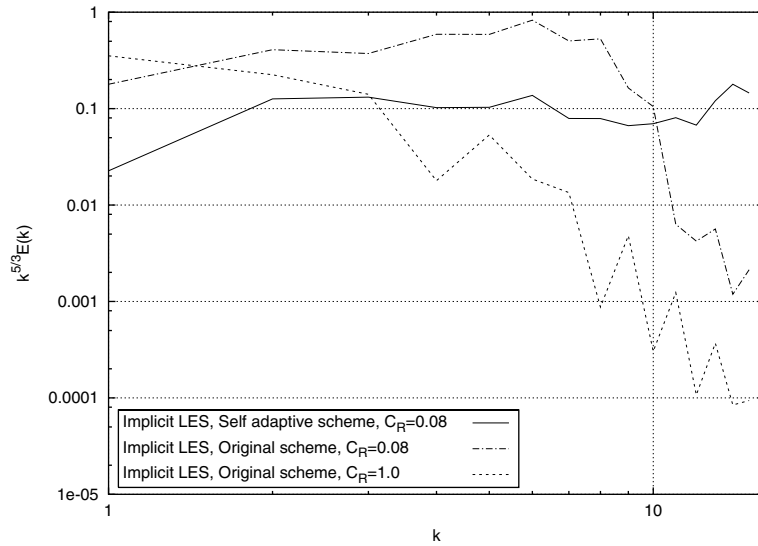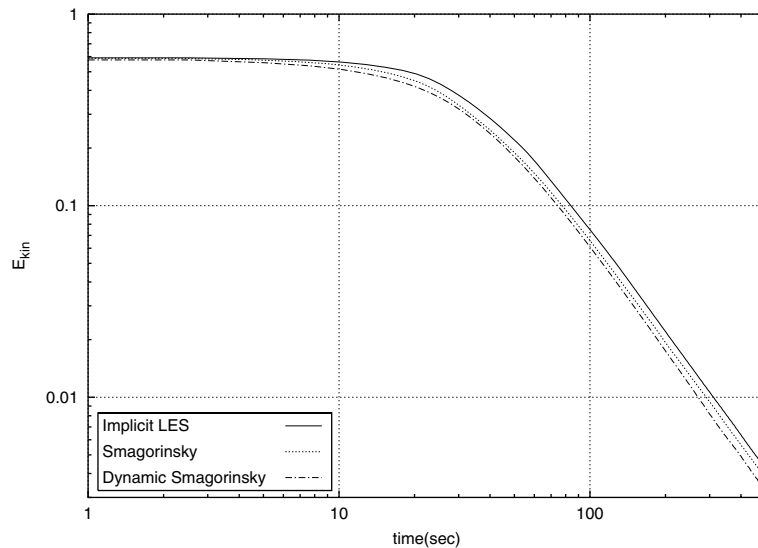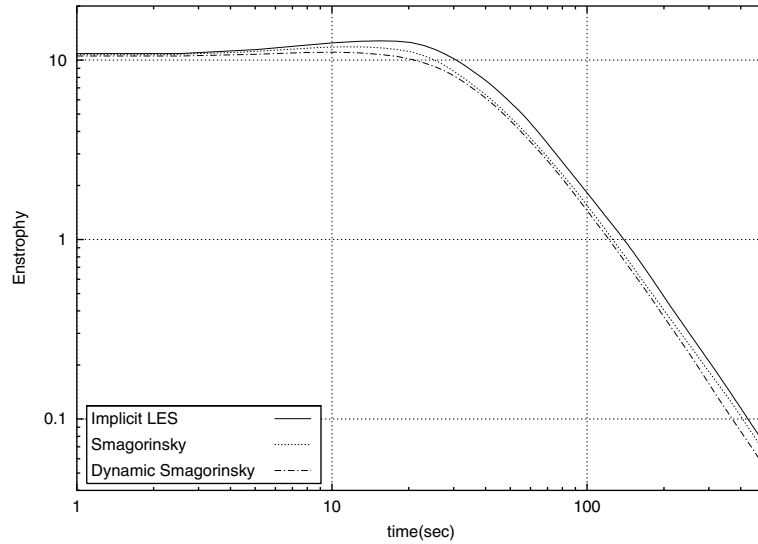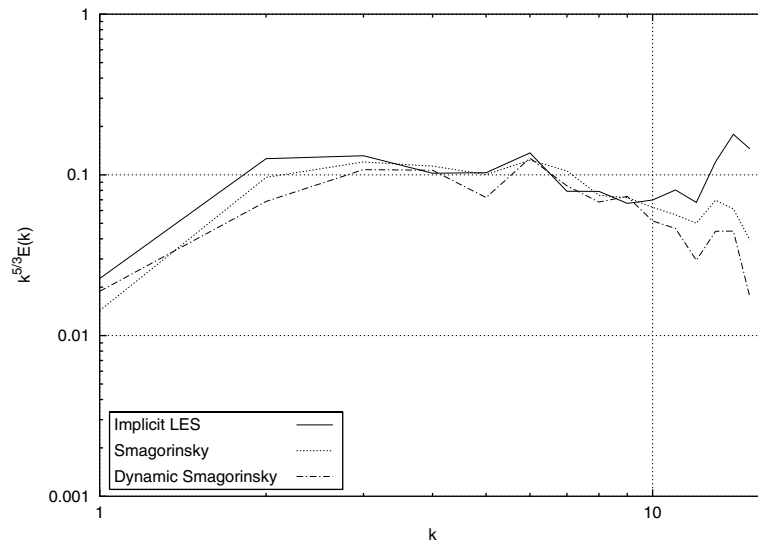Fig. 7. Time history of resolved enstrophy – $32^3$ grid.



Fig. 8. Compensated turbulent kinetic energy spectra at the final stage of the computations – $32^3$ grid.

We consider now the sub-grid scale models implemented. The self-adaptive discretisation scheme is used in all the calculations with the same setup of the previous tests ($C_R = 0.08$, $\Delta_I = \Delta_D = 0.2$). The value of the Smagorinsky coefficient is 0.18, which corresponds to its theoretical value for isotropic turbulence at infinite Reynolds number. Fig. 9 shows the time history of the average artificial smoothing contribution. The results are presented as percentage of the amount of dissipation introduced by the original non-limited version of the scheme. The strong dependance of the self-adaptive discretisation scheme on the sub-grid scale models is evident. After the initial transient all the calculations settle down to an almost constant value,
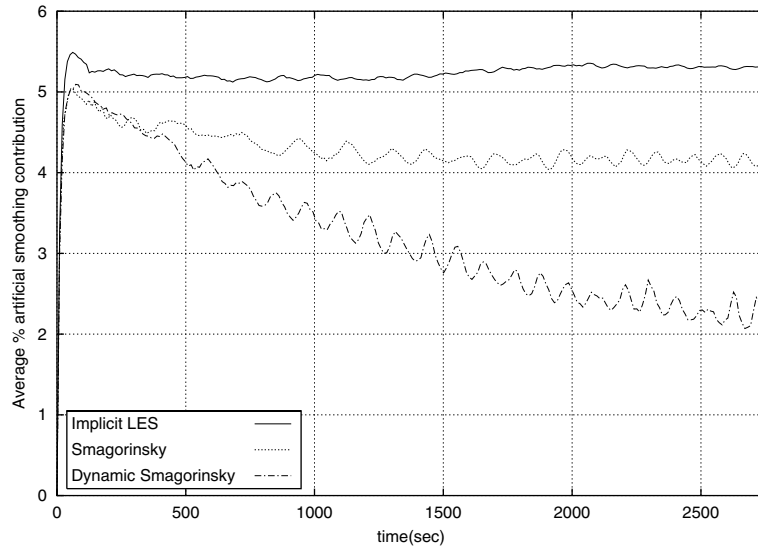
Fig. 9. Time history of average artificial smoothing contribution – $32^3$ grid.

with the dynamic Smagorinsky model producing a lower value than the Smagorinsky model. Not surprisingly the implicit solution has the highest values among all the cases.

Figs. 10–12 show the time history of resolved turbulent kinetic energy, enstrophy and the compensated turbulent kinetic energy spectra at the final stage of the computations. The two models introduced give satisfactory results. They manage to remove the energy pile up at high frequencies, seen in the implicit calculation. They produce a slightly earlier decay of resolved kinetic energy and enstrophy, without affecting the decay rate of resolved kinetic energy, which is still proportional to $t^{-1.61}$.



Fig. 10. Time history of resolved turbulent kinetic energy – $32^3$ grid.

Fig. 11. Time history of enstrophy – $32^3$ grid.



Fig. 12. Compensated turbulent kinetic energy spectra at the final stage of the computations – $32^3$ grid.

The mesh convergence of the simulations has been investigated using a $64^3$ grid. The setup of the discretisation scheme and of the sub-grid scale models have been maintained as for the $32^3$ grid. Figs. 13–15 show the time history of resolved turbulent kinetic energy, enstrophy and the compensated turbulent kinetic energy spectra at the final stage of the computations. The decay rate of resolved kinetic energy is a bit too high for the implicit solution ($t^{-1.68}$) and surprisingly is slightly worse than for the $32^3$ grid. Anyway the scheme has not been optimised for implicit solutions and if we consider the calculations with sub-grid scale models, the increased resolution improves the results. The decay rate for these is in fact
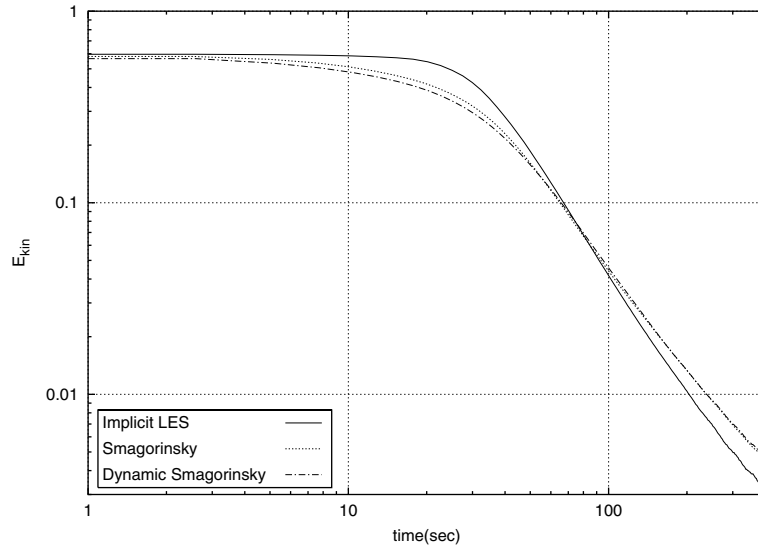
Fig. 13. Time history of resolved turbulent kinetic energy – $64^3$ grid.
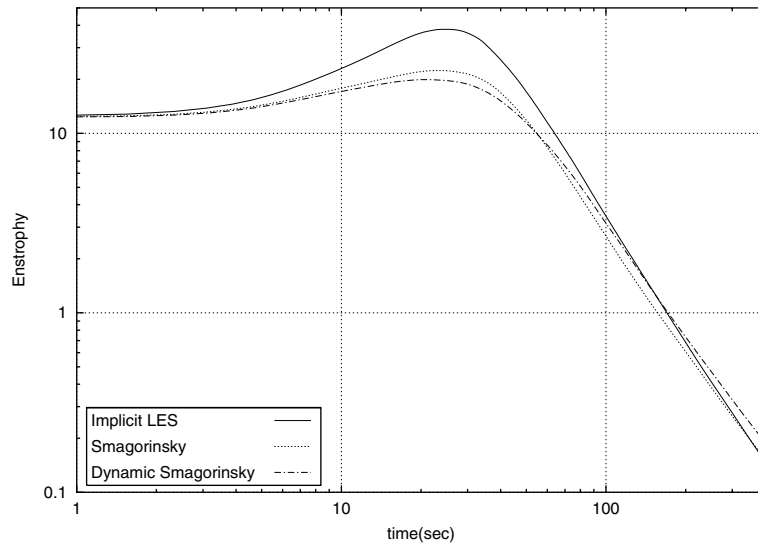


Fig. 14. Time history of enstrophy – $64^3$ grid.

now closer to the theoretical range ($t^{-1.55}$). The energy spectra show again a moderate pile up of energy at the highest frequencies for the implicit calculation, which is removed by the sub-grid scale models. The slope is now close to $k^{-5/3}$ on a wider range than in the calculations performed with the $32^3$ grid. Overall the results obtained with the $32^3$ grid are confirmed, with the sub-grid scale models improving the quality of the solutions.

Since the values of the decay rate of kinetic energy are showing a good trend for the calculations performed with sub-grid scale models at different resolutions but without reaching the theoretical range,
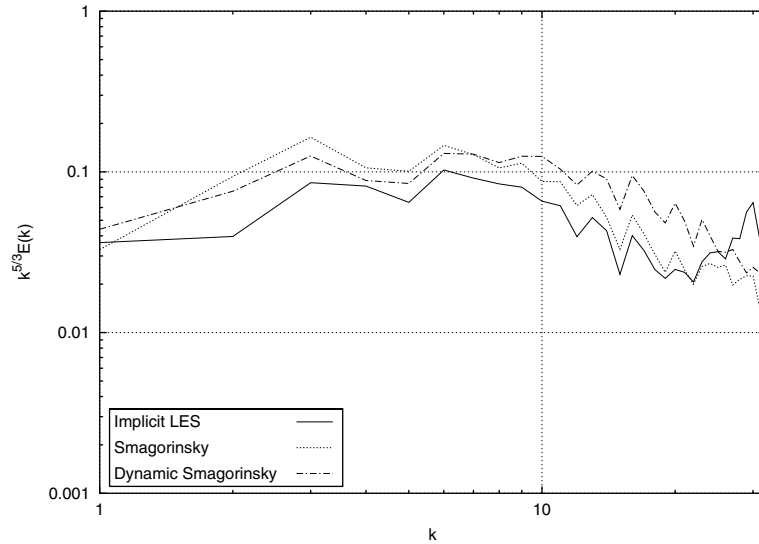
Fig. 15. Compensated turbulent kinetic energy spectra at the final stage of the computations – $64^3$ grid.

a single calculation has been performed using a $96^3$ mesh with the Smagorinsky model. A comparison with the $64^3$ mesh is presented in Fig. 16. The decay rate improves now with the increased resolution from $t^{-1.55}$ to $t^{-1.41}$, showing a good improvement direction.

A significative way to assess the effects of interaction between the discretisation scheme and the sub-grid scale models is by monitoring the effective viscosity $v_e(k|k_c)$. Traditionally eddy viscosities have been compared with spectra computed with analytical theories of turbulence [32]. Domaradzki et al. [33] have recently proposed a method of computing effective viscosity in the context of a MILES calculation. The
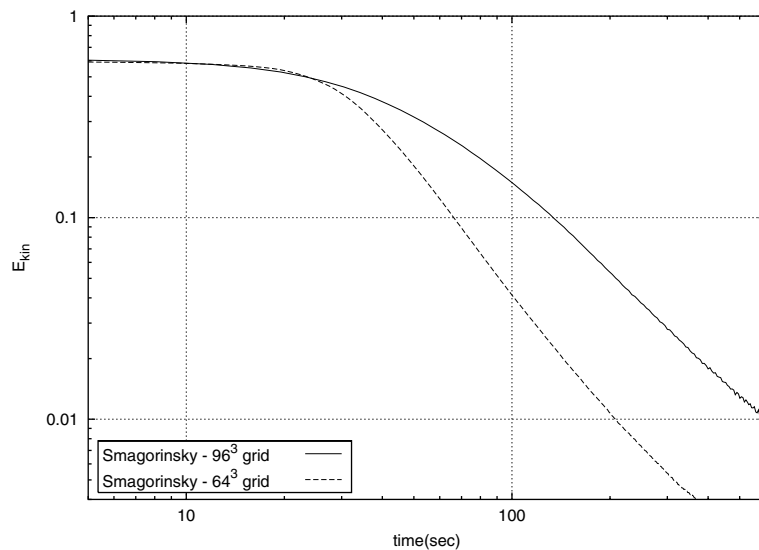


Fig. 16. Time history of resolved turbulent kinetic energy – $64^3$ and $96^3$ grid – Smagorinsky model.

effective viscosity is the equivalent viscosity that represents the energy transfer between the mode $k$ and modes located beyond the cutoff wavenumber $k_c$. It can be defined as:

$$v_e(k|k_c) = -\frac{T(k|k_c)}{2k^2E(k)}, \tag{31}$$

where $T(k|k_c)$ is the energy transfer from the modes of magnitude $k$ to the sub-grid modes. As for the energy spectra, eddy viscosities are integrated over spherical shells and plotted versus the magnitude of the wavenumber. In a LES calculation, the sub-grid scale model (or the artificial dissipation for an implicit solution) provides a dissipative contribution which should be equivalent to $T(k|k_c)$. We can define two separate components $T^{sgs}(k|k_c)$ and $T^{num}(k|k_c)$, associated, respectively, with the sub-grid scale model dissipation and with the numerical dissipation introduced to stabilise the scheme. They can be seen as the Fourier transform of the energy drain caused by two specific forcing terms in the resolved momentum equations: the one associated with the sub-grid scale contribution and the one associated with the smoothing term controlled by the sensor.

$$T^{sgs} = \frac{\partial \tau_{ij}^r}{\partial x_j}\overline{u}_i, \tag{32}$$

$$T^{num} = \frac{\partial \tau_{ij}^{as}}{\partial x_j}\overline{u}_i, \tag{33}$$

where $\tau^{as}$ is the contribution from the artificial smoothing in the momentum equation. Consequently, we can also define two distinct effective viscosities $v_e^{sgs}(k|k_c)$ and $v_e^{num}(k|k_c)$, which sum to a total effective viscosity $v_e^{tot}(k|k_c)$:

$$\begin{aligned} v_e^{sgs}(k|k_c) &= -\frac{T^{sgs}(k|k_c)}{2k^2E(k)}, \\ v_e^{num}(k|k_c) &= -\frac{T^{num}(k|k_c)}{2k^2E(k)} \\ v_e^{tot}(k|k_c) &= -\frac{T^{sgs}(k|k_c) + T^{num}(k|k_c)}{2k^2E(k)}. \end{aligned} \tag{34}$$

Figs. 17 and 18 show the spectra of numerical effective viscosity $v_e^{num}$, sub-grid scale model effective viscosity $v_e^{sgs}$, and total effective viscosity $v_e^{tot}$ for the $32^3$ grid. The analysis of Ghosal [5] is confirmed, with the numerical component being in general dominant over the sub-grid scale component (with the only exception of the lowest frequencies in the Smagorinsky solution). Nevertheless the role of the sub-grid scale models appears to be crucial once again. The effect of interaction between sub-grid scale models and numerical scheme is in fact very strong, producing values of numerical eddy viscosity dramatically different for different sub-grid scale approaches. A general agreement in the trend of the numerical component and the sub-grid scale component is observed for both of the models. This is probably due to the fact that numerical dissipation and sub-grid scale dissipation are triggered by similar flow features. The Smagorinsky model produces higher values for both the numerical and the sub-grid scale component if compared with the dynamic model. The implicit model is obviously under-dissipative on the smallest resolved scales, in agreement with the energy spectra shown previously.

In order to obtain a further insight into the effect of the sub-grid scale models, a new set of calculations was started from a same set of initial flow conditions. Flow conditions at the end of the calculation with the dynamic Smagorinsky sub-grid scale model were chosen. The plots of effective viscosities are extracted after a single time iteration and are presented in Fig. 19. The lower values produced by the dynamic model are the consequence of the initial flow conditions being produced by a dynamic
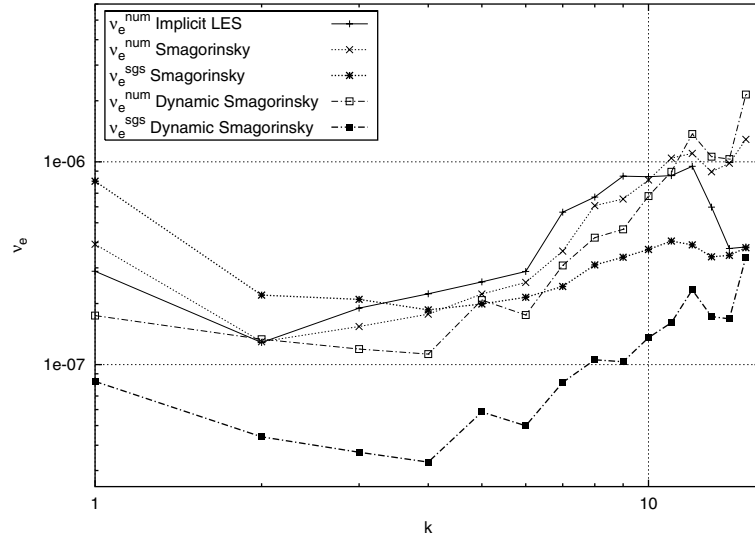
Fig. 17. Spectra of numerical effective viscosity ($\nu_e^{num}$) and sub-grid scale model effective viscosity ($\nu_e^{sgs}$) – $32^3$ grid.
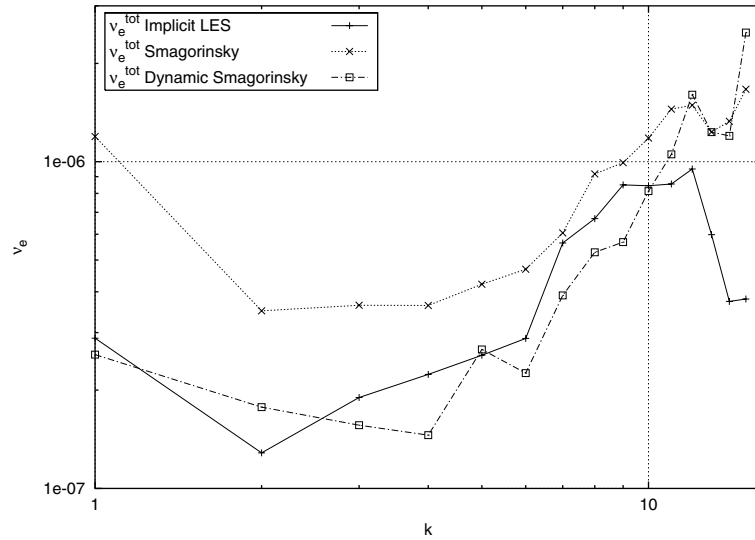


Fig. 18. Spectra of total effective viscosity ($\nu_e^{tot}$) – $32^3$ grid.

Smagorinsky calculation. In contrast to Fig. 18, the numerical dissipation has now a significant value also for the smallest resolved scales. Therefore, the inability of the implicit solution to introduce a sufficient amount of dissipation in this range is a consequence of the lack of a sub-grid scale component in the long term.

In order to assess the effect of the new discretisation scheme for wall bounded flows a test on fully developed channel flow at friction Reynolds number $Re_\tau = 395$ has been performed. The domain considered has dimension $2\pi$ in streamwise direction, $\pi$ in sidewise direction and 2 in wall normal direction. The mesh resolution is $64 \times 64 \times 64$. Only implicit calculations are considered at this stage, therefore $C_R$ is
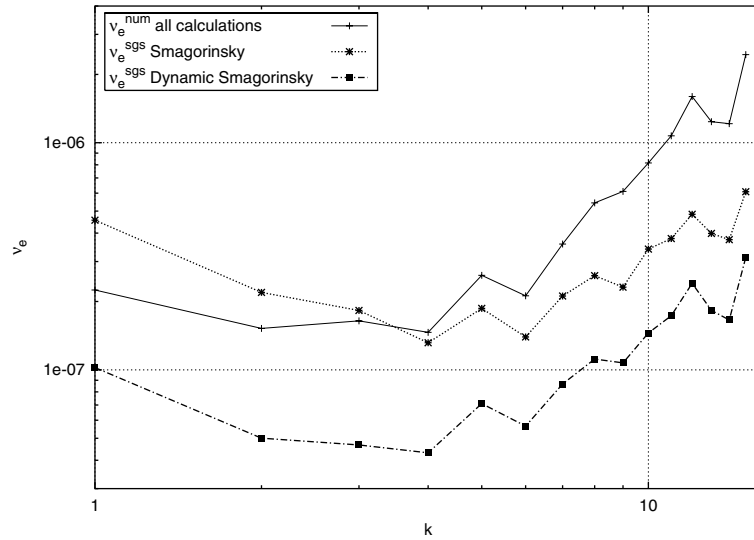
Fig. 19. Numerical effective viscosity ($v_e^{num}$) and sub-grid scale model effective viscosity ($v_e^{sgs}$) – $32^3$ grid – calculations restarted from decayed dynamic Smagorinsky flow condition.

increased to 0.3 for both of the schemes (the original without sensor and the new self-adaptive scheme), in the attempt to compensate for the missing sub-grid scale model. DNS data from Moser et al. [34] is used for comparison.

A calculation without any artificial smoothing contribution ($C_R = 0.0$) was also attempted but became unstable after few iterations. Results are presented in Figs. 20–23.
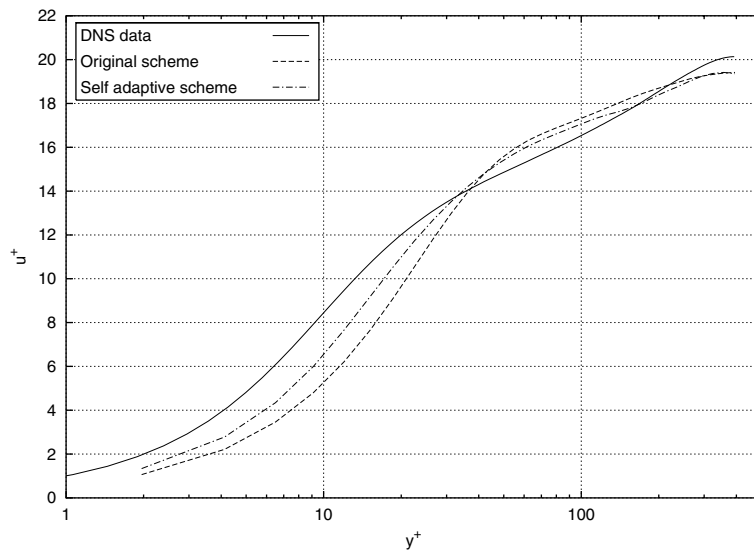


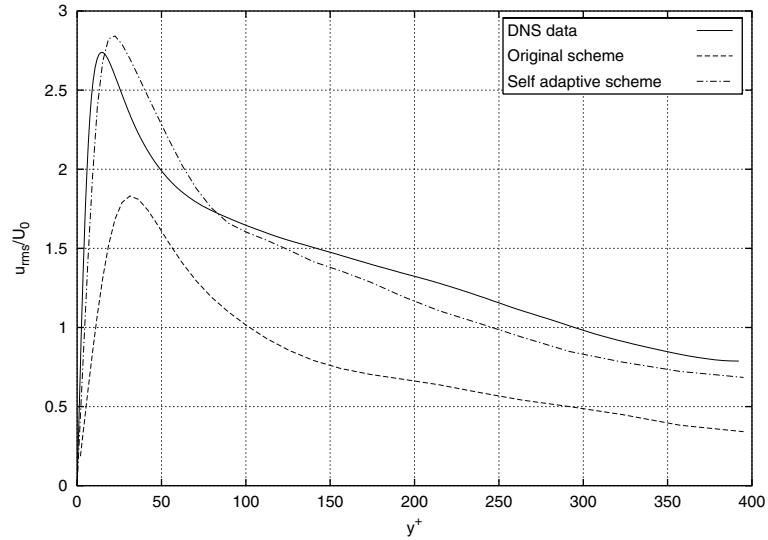Fig. 20. Fully developed channel flow, $Re_\tau = 395$, mean velocity profile in wall coordinates.

Fig. 21. Fully developed channel flow, $Re_\tau = 395$, rms $u$ velocity profile in wall coordinates.
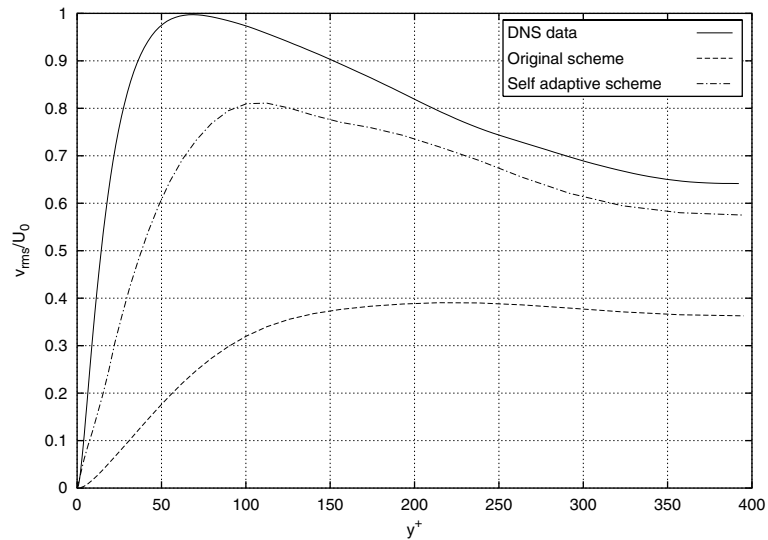


Fig. 22. Fully developed channel flow, $Re_\tau = 395$, rms $v$ velocity profile in wall coordinates.

The self-adaptive scheme offers a considerably better comparison with the DNS data, in particular for the *rms* components. The agreement with DNS is in this case quite good, in particular considering the mesh resolution. In general, the position of the peaks and level of fluctuations are close to the DNS data. Streamwise fluctuations are slightly overpredicted, while fluctuations in wall-normal and sidewise directions are underpredicted, as expected with this mesh resolution. Results could probably be further improved introducing a sub-grid scale model or using a finer mesh. The original scheme proves once again to be too dissipative.
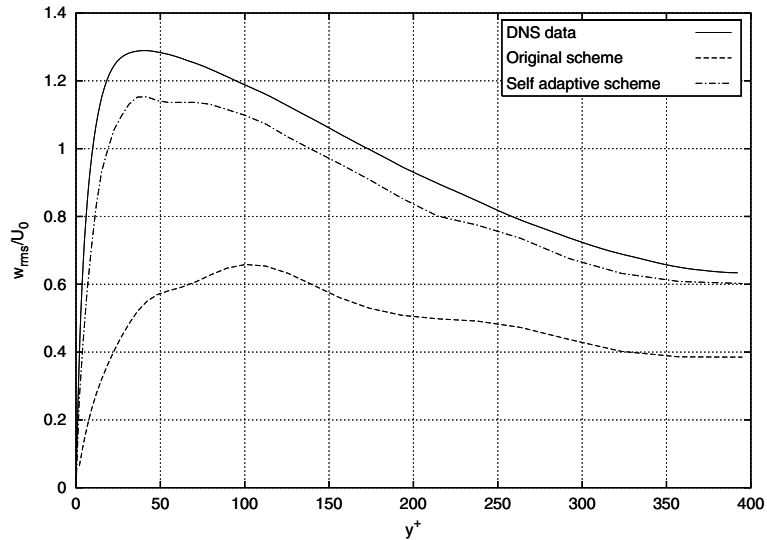
Fig. 23. Fully developed channel flow, $Re_\tau = 395$, rms $w$ velocity profile in wall coordinates.

## 6. Conclusions

A self-adaptive discretisation scheme in the context of an unstructured finite-volume flow solver has been introduced. The strategy adopted tries to minimise the contribution of artificial dissipation, relying on a sensor that detects wiggles in the flow variables. Tests on decaying isotropic turbulence at infinite Reynolds number have been performed comparing this new scheme with the original non-limited version. Encouraging results have been obtained. When used for implicit LES, the original scheme appears to be overdissipative, preventing any sub-grid scale model from producing a proper LES solution. On the other hand, the new scheme produces considerably better resolved kinetic energy and enstrophy time histories. The energy spectra present an extensive region in good agreement with the theoretical slope of the inertial range and a moderate energy pile up at the highest resolved frequency. A specific tuning of the scheme could probably improve this aspect, producing better implicit solutions.

The Smagorinsky and the dynamic Smagorinsky sub-grid scale models have been implemented and coupled with the self-adaptive discretisation scheme. Both of the models improve significantly the results. They manage to produce the right amount of dissipation for the highest resolved frequencies and to some extent to improve the time history of resolved kinetic energy.

An explicit filter has been used for the dynamic model. It is one of the first applications of a discrete interpolation filter based on the approach presented by Marsden et al. An original procedure to impose the filter shape, through a specific selection process of the basic filters, has also been proposed.

Overall the main conclusion drawn from the tests on decaying isotropic turbulence is the fact that the strong effect of the models is produced despite the numerical dissipation being dominant over the sub-grid scale dissipation (as expected for a second-order unstructured implementation).

A test on fully developed channel flow at $Re_\tau = 395$ was also performed using implicit LES, in order to assess the effect of the new discretisation scheme for wall bounded flows. Once again the introduction of the limiter proved to be beneficial.

## Acknowledgements

## References

[1] P. Sagaut, Large Eddy Simulation for Incompressible Flows: An Introduction, second ed., Springer, Berlin, 2002.

[2] B.J. Geurts, Elements of Direct and Large-eddy Simulation, Edwards, 2003.

[3] M. Ciardi, W.N. Dawes, Large eddy and detached eddy simulations for broadband noise prediction in complex geometries, in: Friedrich, Geurts, Metais (Eds.), Direct and Large Eddy Simulation V, Kluwer Academic Publishers, Dordrecht, 2004.

[4] P. Sagaut, LES and DNS simulation of turbomachinery flows, Recent developments in numerical methods for turbomachinery flows, VKI Lecture, November, 2001.

[5] S. Ghosal, An analysis of numerical errors in large-eddy simulations of turbulence, Journal of Computational Physics 125 (1996) 187–206.

[6] J.P. Boris, F.F. Grinstein, E.S. Oran, R.L. Kolbe, New insights into large eddy simulation, Fluid Dynamic Research 10 (1992) 199–228.

[7] E. Garnier, M. Mossi, P. Sagaut, P. Comte, M. Deville, On the use of shock-capturing schemes for large-eddy simulation, Journal of Computational Physics 153 (1999) 273–311.

[8] H. Yan, D. Knight, Large-eddy simulation of supersonic flat-plate boundary layers using monotonically integrated large eddy simulation (MILES) technique, Journal of Fluids Engineering 124 (2002) 868–875.

[9] T.K. Sengupta, M.T. Nair, Upwind schemes and large eddy simulation, International Journal for Numerical Methods in Fluids 31 (1999) 879–889.

[10] F.K. Chow, P. Moin, A further study of numerical errors in large-eddy simulations, Journal of Computational Physics 184 (2003) 366–380.

[11] S.B. Pope, Turbulent Flows, Cambridge University Press, Cambridge, 2000.

[12] A.L. Marsden, O.V. Vasilyev, P. Moin, Construction of commutative filters for LES on unstructured meshes, Journal of Computational Physics 175 (2002) 584–603.

[13] A.L. Marsden, O.V. Vasilyev, Commutative filters for LES on unstructured meshes, Annual Research Briefs-1999 389-402, CTR, Stanford University, 1999.

[14] B.J. Geurts, Balancing errors in LES, in: Voke, Sandham, Kleiser (Eds.), Direct and Large Eddy Simulation III, Kluwer Academic Publishers, Dordrecht, 1999.

[15] B. Vreman, B. Geurts, H. Kuerten, A priori tests of large eddy simulation of the compressible plane mixing layer, Journal of Engineering Mathematics 29 (1995) 299–327.

[16] B. Vreman, B. Geurts, H. Kuerten, A finite volume approach to large eddy simulation of compressible homogeneous, isotropic, decaying turbulence, International Journal for Numerical Methods in Fluids 15 (1992) 799–816.

[17] L. Martinelli, Calculations of viscous flows with a multigrid method, Ph.D. Thesis, Department of Mechanical and Aerospace Engineering, Princeton University, 1997.

[18] P.L. Roe, Approximate Riemann solvers, parameter vectors, and difference schemes, Journal of Computational Physics 43 (1981) 357–372.

[19] P.I. Crumpton, P. Moinier, M.B. Giles, An unstructured algorithm for high Reynolds number flows on higly stretched grids, in: Taylor, Cross (Eds.), Numerical Methods in Laminar and Turbulent Flow, Pineridge Press, 1997, pp. 561–572.

[20] C. HirschNumerical Computation of Internal and External Flows, vol. 2, Wiley, New York, 1990.

[21] P. Moinier, M.B. Giles, Preconditioned Euler and Navier–Stokes calculations on unstructured grids, in: 6th ICFD Conference on Numerical Methods for Fluid Dynamics, Oxford, UK, 1998.

[22] P. Moinier, Algorithm developments for an unstructured viscous flow solver, Ph.D. Thesis, University of Oxford, UK, 1999.

[23] F. Ducros, V. Ferrand, F. Nicoud, C. Weber, D. Darracq, C. Gacherieu, T. Poinsot, Large-eddy simulation of the shock–turbulence interaction, Journal of Computational Physics 152 (1999) 517–549.

[24] I. Mary, P. Sagaut, Large eddy simulation of flow around an airfoil near stall, AIAA Journal 40 (6) (2002) 1139–1145.

[25] J. Smagorinsky, General circulation experiments with the primitive equations: I. The basic equations, Monthly Weather Review 91 (1963) 99–164.

[26] M. Germano, Turbulence: the filtering approach, Journal of Fluid Mechanics 238 (1992) 325–336.

[27] D.K. Lilly, A proposed modification of the Germano subgrid-scale closure method, Physics of Fluids 4 (3) (1992) 633–635.

[28] C. Fureby, F.F. Grinstein, Monotonically integrated large eddy simulation of free shear flows, AIAA Journal 37 (5) (1999) 544–556.

[29] F.F. Grinstein, C. Fureby, Recent progress on MILES for high Reynolds number flows, Journal of Fluids Engineering 124 (2002) 848–861.

[30] C. Fureby, F.F. Grinstein, Large eddy simulation of high-Reynolds-number free and wall-bounded flows, Journal of Computational Physics 181 (2002) 68–97.

[31] J. Bardina, J.H. Ferziger, W.C. Reynolds, Improved subgrid scale models for large eddy simulations, AIAA Paper 80, 1980, 1357.

[32] M. Lesieur, Turbulence in Fluids, second ed., Kluwer Academic Publishers, Dordrecht, 1990.

[33] J.A. Domaradzki, Z. Xiao, P.K. Smolarkiewicz, Effective eddy viscosities in implicit large eddy simulations of turbulent flows, Physics of Fluids 15 (12) (2003) 3890–3893.

[34] R.D. Moser, J. Kim, N.N. Mansour, Direct numerical simulation of turbulent channel flow up to $Re_\tau = 590$, Physics of Fluids 11 (4) (1999) 943–945.